TU Delft

Delft University of Technology

Railway bridge dynamics considering piled foundations in soft soil

Peng, Borong; Xu, Lei; Connolly, David P.; Li, Zheng; He, Xuhui; Xiao, Yuanjie; Guo, Yunlong

DOI
10.1016/j.soildyn.2024.108844

Publication date
2024

Document Version
Final published version

Published in
Soil Dynamics and Earthquake Engineering

Citation (APA)
Peng, B., Xu, L., Connolly, D. P., Li, Z., He, X., Xiao, Y., & Guo, Y. (2024). Railway bridge dynamics considering piled foundations in soft soil. *Soil Dynamics and Earthquake Engineering*, *184*, Article 108844. https://doi.org/10.1016/j.soildyn.2024.108844

Important note
To cite this publication, please use the final published version (if applicable).
Please check the document version above.

Copyright
Other than for strictly personal use, it is not permitted to download, forward or distribute the text or part of it, without the consent of the author(s) and/or copyright holder(s), unless the work is under an open content license such as Creative Commons.

Takedown policy
Please contact us and provide details if you believe this document breaches copyrights.
We will remove access to the work immediately and investigate your claim.

This work is downloaded from Delft University of Technology.
For technical reasons the number of authors shown on this cover page is limited to a maximum of 10.

Soil Dynamics and Earthquake Engineering 184 (2024) 108844

Contents lists available at ScienceDirect

Soil Dynamics and Earthquake Engineering

journal homepage: www.elsevier.com/locate/soildyn

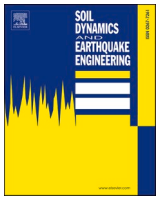

Railway bridge dynamics considering piled foundations in soft soil

Borong Peng [a], Lei Xu [a,d], David P. Connolly [b], Zheng Li [a,**], Xuhui He [a,d], Yuanjie Xiao [a,d], Yunlong Guo [c,e,*]

[a] School of Civil Engineering, Central South University, Changsha, 410075, Hunan, China
[b] School of Civil Engineering, University of Leeds, Leeds, LS2 9JT, United Kingdom
[c] Faculty of Civil Engineering and Geosciences, Delft University of Technology, Delft, 2628CN, Netherlands
[d] National Engineering Research Center of High-speed Railway Construction Technology, Changsha, 410075, China
[e] Department of Civil Engineering, School of Engineering, University of Birmingham, Birmingham, B152TT, United Kingdom

ARTICLE INFO

Keywords:
Train-track-bridge interaction
Pile-soil interaction
Dynamic railway system
Finite element modeling
Railway bridge engineering

ABSTRACT

The dynamic response of a railway bridge can be affected by the properties of its foundations, particularly if founded on soft soils. Thus, this work aims to establish a coupled dynamic model to investigate the vibration of train-track-bridge systems considering piled foundations embedded in soft soil. Firstly, to construct the simulation framework, the finite element and multi-body methods are used to model the dynamic behavior of a train-track-bridge interaction (TTBI) system and a pier-cap-pile-soil interaction system. The equilibrium of the two sub-systems is maintained through the bridge's bearing force and a multi-time-step integration strategy is introduced to improve computational efficiency. The proposed model is validated by comparing it to the results from commercial finite element software ABAQUS. Then results are computed using the proposed model and the conventional TTBI model without piles. It is concluded that when considering the piled foundations, the low-frequency vibration of the TTBI system is dominant. Moreover, the vibration energy in the track and bridge below 7 Hz is larger compared with the conventional TTBI model. The influence of train speed on the vibration characteristics of the pile and soil is analyzed. It is found that higher train speeds cause increased pile and soil accelerations at the frequencies associated with the train axle spacing. The novelty of the analysis is providing a new insight into the coupled vibration properties of TTBI systems considering the participation of piled foundations in soft soil.

1. Introduction

For piled bridge foundations subject to cyclic train loads, the low stiffness of the surrounding soil causes increased dynamic vibration, which can affect the dynamic stability of train. Therefore it is necessary to analyze train-induced vibrations of track-bridge structures and piled foundations under soft soil conditions.

Train-track-bridge interaction (TTBI) describes the dynamic behavior of trains passing over bridges [1,2]. It is a challenge to study the multiple complex interactions between the different parts of the system. For example, the periodicity of the bridge girders makes the response of the full TTBI system quite different compared to conventional train-track interaction. In an attempt to numerically model the problem, Matsuura [3–5] simulated the vehicle as a multi-body with two suspension systems, and the bridge using classical beam theory. The resonance between the vehicle and bridge was studied and prediction formulae for train resonance speed were proposed. Alternatively, Tanabe and Yamada [6] established a train-track-bridge coupled model using the finite element (FE) method, while Li et al. [7] established a train-track-long-span steel cable-stayed bridge interaction model, in which the girder disturbance and train riding comfort/safety under various train speeds were studied. Zeng et al. [8] adopted localized Lagrange multipliers to establish a dynamic analysis approach for vehicle-bridge interaction, which enabled the partitioned, non-iterative, dynamic analysis of the vehicle and the bridge subsystems. Alternatively, Azimi et al. [9] proposed a new formulation to capture bridge and vehicle response more realistically considering the structural properties of vehicle-bridge interaction elements. Xin et al. [10] adopted the modal superposition method and Fourier series expansion to calculate the vibration of the bridge. Then the semi-analytical solution of the bridge

* Corresponding author.
** Corresponding author.
E-mail addresses: lizheng0924@csu.edu.cn (Z. Li), yunlong.guo@tudelft.nl (Y. Guo).

https://doi.org/10.1016/j.soildyn.2024.108844
Received 19 April 2024; Received in revised form 11 June 2024; Accepted 9 July 2024
Available online 15 July 2024
0267-7261/© 2024 The Authors. Published by Elsevier Ltd. This is an open access article under the CC BY license (http://creativecommons.org/licenses/by/4.0/).

vibrations under moving train loads was derived. It was then extended to the dynamic analysis of systems under multi-source excitation, such as earthquakes and crosswinds [11,12].

At present, a precise model describing wheel-rail contact has been introduced into the modelling framework of the TTBI. For example, Zhai and Wang et al. [13,14] established a coupled dynamic model for studying the dynamic behavior of the TTBI considering the excitation of track irregularities. In their model, the so-called "trace line method" was used to depict the normal and tangent contact between wheel and rail, and the coupled vibration properties of the TTBI were analyzed. Luo et al. [15] implement track flexibility and advanced coupling relations into a three-dimensional train-slab track system to perform in-depth train-track interaction study.

Recently, with advancements in theoretical models and computational techniques, more complex substructures have been considered in the simulation of train-induced vibration. For example, Yang et al. [16] established a train-track-soil dynamic model to investigate building vibrations induced by trains and complex numerical models for tunnel-soil and building interaction. Also, in Refs. [17,18], numerical models of bridge-tunnel and bridge-subgrade transition zones are established to study the influence of uneven stiffness on train-induced vibrations. However, there are limited works on the coupled analysis of train-track-bridge-pile-soil interaction. Generally, most research has studied the vibration of piled foundations and wave propagation in the surrounding soil. For example, Zhang et al. [19] establish a nonlinear analysis model of pile-soil interaction considering frozen soil effects, to study pier dynamic response under earthquakes. Further, Chen et al. [20] proposed a simplified numerical modelling method for soil-water-structure modelling, to analyze the dynamic response of piles under near-field and far-field earthquake conditions.

Considering the aforementioned literature, pile-soil substructure is rarely considered in the simulation of the train-induced vibrations. However, the interaction forces from bridge piers are transmitted into the piled foundations, and generate feedback to the TTBI system, which influences the dynamic performance of the train and other components. Li et al. [21] introduced the effect of pile-soil interaction into the TTBI, where the FE method was used to simulate pile-soil coupling behavior assuming a displacement continuity condition. In their work, the influence of bearing stiffness on ground vibration induced by trains moving the bridge was studied, while in further research [22], a semi-analytical approach was explored. Shan et al. [23] simulated the foundation soil as a spring to simulate the pile-soil interaction in frozen soil areas. Liang et al. [24] used a modified "P–Y curve method" and "load transfer hyperbola method" to study the nonlinear behavior of pile-soil interaction. Romero et al. [25,26] established a three-dimensional FE model of a single-span simply supported beam bridge considering the effects of pile and soil, in which the soil was considered as a half-space. The resonant characteristics of the bridge under different soil stiffness were investigated. Shamsi M.G et al. [27] establish an advanced three-dimensional (3D) continuum finite element under a moving train and then analyze the critical speed for a particular soil-bridge condition.

Considering the state-of-the-art of the TTBI and soil-pile interaction field, there remain some challenges.

(1) **Non-coupled dynamic analysis of the system:** Conventional co-simulation approaches based on commercial software are typically an uncoupled system. The interaction forces of the two separated dynamic systems are not in equilibrium when using substructure methods.
(2) **More accurate description of the pile-soil interaction:** It is common that the properties of the contact surface of the pile-soil are simplified using a "common-node" approach. A more accurate model should be established to depict the contact and slippage behaviors of the pile-soil contact surface.

To address these issues, a coupled train-track-bridge-pier-cap-pile-soil interaction (TTBPCPSI) model is established to investigate the coupled vibration properties of the TTBI system considering a soft soil support. The basic dynamic model is established by introducing a fully 3D pile-soil interaction model into the TTBI model. The contact slippage behaviors of the pile-soil contact surface are simulated using contact elements. The following parts of the manuscript are organized as: **Section 2**: the model for simulating train-track interaction and detailed formulations for pile-soil interaction; **Section 3**: the pile-soil dynamic model is validated by comparing it to results calculated using commercial FE software; **Section 4**: two illustrative examples are used to analyze the vibration behavior of the TTBPCPSI system.

2. Modeling of the TTBPCPSI system

In this section, the train-track-bridge dynamic model and the pile-soil dynamic model are established using FEM.

2.1. Model configuration

As shown in Fig. 1, the approach consists of two sub-models, namely the TTBI model (Fig. 1(a)) and the piled foundations model (Fig. 1(b)). The train-track-bridge dynamic model consists of the high-speed train model, the ballastless track model including rails, track slab, and baseplate, and the bridge system. The train is modeled as a multi-rigid body system, each vehicle is regarded as a multi-rigid-body system with 42 degrees of freedom (DOFs), including the bodies of one car body, two bogie frames, and four wheelsets. Each rigid body has six degrees of freedom: vertical-, lateral-, yaw-, pitch- and rolling-motions, as shown in Fig. 3. In the flexible ballastless track and bridge models, the rail is simulated using Euler beam elements, while the track slab and baseplate and the bridge deck are simulated using Mindlin plate elements, as shown in Fig. 2(a) and 4. The interaction between each component is simulated using spring-dashpot elements via a multi-scale coupling technique [28]. The coupling of the train and track is implemented using a wheel-rail interaction model which accounts for the spatial contact relationship between wheel and rail [29]. The mechanical parameters of the train, track, and bridge system are listed in Appendix Tables 1, 2 and 3, respectively. The pile and surrounding soil are modeled using 8-node solid elements, and their interfaces are modeled using Desai contact elements [30,31] (Fig. 2(b)). The modeling of the train-track-bridge model has been elaborated in previous works [32], meaning the emphasis of this paper is placed on the modeling of pile-soil interaction

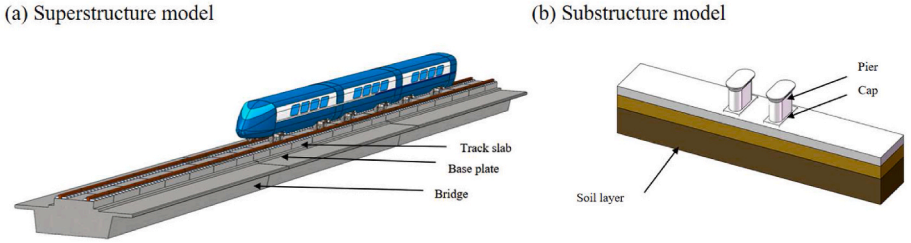

Fig. 1. Overview of the TTBPCPSI system (a) superstructure model (b) substructure model.

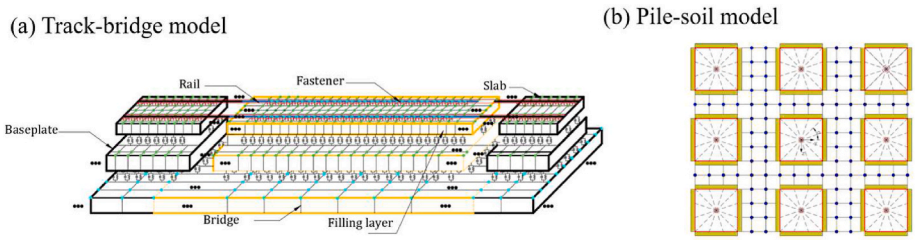

Fig. 2. Mathematical model (a) TTBI model (b) pile-soil model.

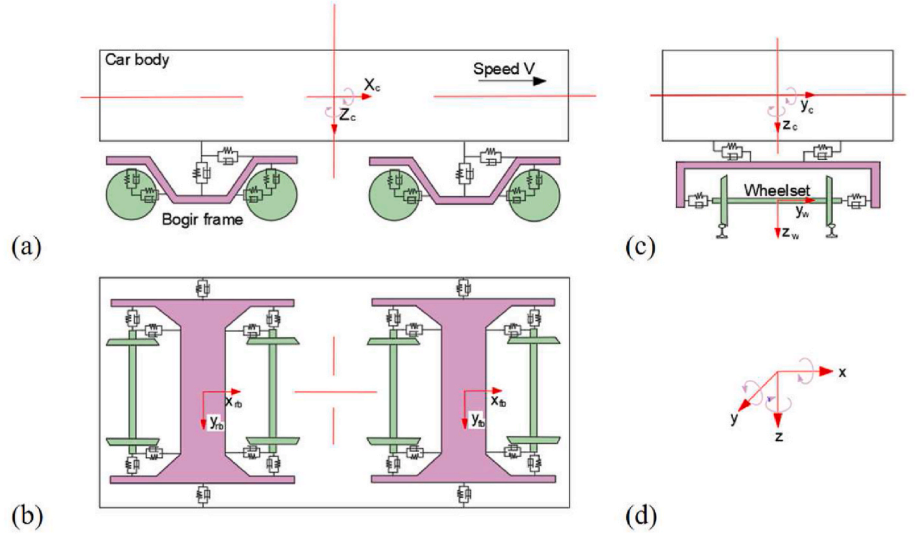

Fig. 3. Representation of the vehicle model (a. side view; b. end view; c. top view; d. coordinate system).

model and the solution of the coupled models. Using MATLAB, codes were developed to establish the model and solve it.

2.2. Coupling of the bridge-bearing system

In contrast to the more common method used in pier-cap surface and cap-pile surface simulation, the interactions between the track slab-filling layer, the filling layer-base plate, the base plate-bridge deck and the bridge-pier are simulated by using springs and dampers, with the parameters in Appendix Table 4. Taking the interaction between the pier and bridge, as an example, as shown in Fig. 4. The bearing is simulated as spring and damping. The location of the bearing is defined according to the design of 32 m simple-supported beam bridge in China. In addition, it needs to transform the global coordinates into the local coordinates of the element and then the coupled stiffness and damping spring can be established based on the principle of energy variation, given by:

$$\begin{cases} K_{bp} = k_{bearing} H_{br} W_{br} \left[N_{bp}\right]^T \left[N_{bp}\right] \\ C_{bp} = c_{bearing} H_{br} W_{br} \left[N_{bp}\right]^T \left[N_{bp}\right] \end{cases} \tag{1}$$

with

$$\left[\mathrm{N}_{bp}\right] = \left[\mathrm{N}_b(x,y) - \mathrm{N}_p(\tilde{x},\tilde{y})\right];$$

where N_b and N_p represent the shape function of bridge and pier respectively; H_{br} and W_{br} represent the length and width of bearing respectively; $\tilde{x}$ and $\tilde{y}$ represent the end of the pier in element coordinates; x and y represent the central point of bearing projected

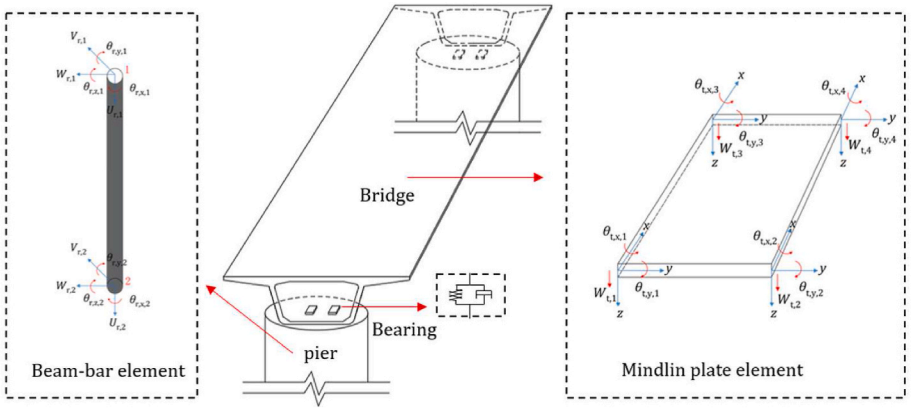

Fig. 4. The schematic of bridge-pier interaction.

vertically to the corresponding the position of bridge in element coordinate; $k_{bearing}$ and $c_{bearing}$ represent the stiffness and the damping of bearing, respectively.

2.3. The coupling of the train and track system

The coupling of the train and track subsystems is modeled based on the fundamental theory of *vehicle-track coupled dynamics* [29]. The coupled wheel-rail interaction matrix consists of the normal non-linear Hertzian contact force and the tangent creep force. The profiles of the wheel and rail are considered, as shown in Fig. 5. More details about the modeling approach are discussed in Ref. [33].

Based on the above, the train–track interaction model can be formulated in matrix form:

$$\begin{bmatrix} M_{VV} & 0 \\ 0 & M_{TT} \end{bmatrix} \begin{Bmatrix} \ddot{X}_V \\ \ddot{X}_T \end{Bmatrix} + \begin{bmatrix} C_{VV} & C_{VT} \\ C_{TV} & C_{TT} \end{bmatrix} \begin{Bmatrix} \dot{X}_V \\ \dot{X}_T \end{Bmatrix} + \begin{bmatrix} K_{VV} & K_{VT} \\ K_{TV} & K_{TT} \end{bmatrix} \begin{Bmatrix} X_V \\ X_T \end{Bmatrix} = \begin{Bmatrix} F_V \\ F_T \end{Bmatrix} \tag{2}$$

where M, C and K denote the mass, damping, and stiffness matrices, respectively; F denotes the loading vector; $\ddot{X}$, $\dot{X}$, and X denote the acceleration, velocity, and displacement vectors, respectively; the subscripts "V" and "T" represent the track and train, respectively.

2.4. Modeling of the pile-soil interaction system

The pile foundation is represented using regular quadrilateral elements with symmetry nodes, as shown in Fig. 6. Firstly, the position of the pile corresponding to the element on the X–Y plane is searched, and then by removing the element stiffness of the soil at the corresponding position of the pile, the overall stiffness matrix of the soil is formed.

The pile element and the corresponding soil element are connected through a contact element to realize pile-soil coupling. The soil boundary is treated using an artificial viscoelastic boundary [34] to eliminate wave reflection, as shown in (Fig. 6(a)), where the equations of the viscous damper and linear spring implemented at the boundary can be written as follows:

$$\begin{cases} K_{bt} = \alpha_t \dfrac{G}{R}, K_{bn} = \alpha_n \dfrac{G}{R} \\ C_{bt} = \rho C_s, C_{bn} = \rho C_p \end{cases} \tag{3}$$

where K_{bt} and K_{bn} denote the tangential and normal stiffness of the spring element respectively; C_{bt} and C_{bn} denote the tangential and damping stiffness of the spring element respectively; C_p and C_s are the symbol of the P wave and S wave propagating in the soil respectively; ρ is the medium mass. The cross-section of meshing layered soil is shown in Fig. 7 and the pile-soil parameters are listed in Appendix Tables 5 and 6

Eight-node Desai thin-layer elements are used to simulate the contact interface of the pile and soil, where the contact surface is divided into the upper and lower planes along the normal direction (Fig. 6(b)). The thickness of the contact element is between 0.1 and 0.01 of the its elemental length. The contact surface consists of the soil around the pile with a small thickness, assuming the strain normal to the contact surface is uniformly distributed along it. The element strain is expressed by the relative displacement of the corresponding nodes (e.g., nodes 1 and 5) on the upper and lower surfaces of the contact surface element. The relative displacement is:

$$\Delta U = \begin{Bmatrix} \Delta u \\ \Delta v \\ \Delta w \end{Bmatrix} = \begin{Bmatrix} \sum_{i=1}^{4} N_i (u_i - u_{i+4}) \\ \sum_{i=1}^{4} N_i (v_i - v_{i+4}) \\ \sum_{i=1}^{4} N_i (w_i - w_{i+4}) \end{Bmatrix} = N \begin{Bmatrix} u_1 \\ v_1 \\ w_1 \\ \vdots \\ u_5 \\ v_5 \\ w_5 \\ \vdots \end{Bmatrix} \tag{4}$$

with

$$N = \begin{bmatrix} N_1 & 0 & 0 & \cdots & N_4 & 0 & 0 & \cdots & -N_4 & 0 & 0 \\ 0 & N_1 & 0 & \cdots & 0 & N_4 & 0 & \cdots & 0 & -N_4 & 0 \\ 0 & 0 & N_1 & \cdots & 0 & 0 & N_4 & \cdots & 0 & 0 & -N_4 \end{bmatrix}$$

$$N_i = \frac{(1 + \xi_i \xi)(1 + \eta_i \eta)}{4}, i = 1, 2, 3, 4,$$

where the displacement parameters, u_i, v_i, and w_i represent the motions along the *x*-, *y*-, and *z*-axes respectively, as shown in Fig. 8. N_i denotes the shape functions with the local coordinate parameters "ξ" and "η".

The strain at any point on the contact surface element can be expressed as the ratio of the normal and tangential relative displacements to the thickness of the contact surface in the coordinate system. Taking the contact element in Fig. 6(b) as an example, the corresponding strain formula is calculated as:

$$\boldsymbol{\varepsilon} = \begin{Bmatrix} \gamma_{xy} \\ \varepsilon_y \\ \gamma_{yz} \end{Bmatrix} = \frac{1}{t} \begin{Bmatrix} \Delta u \\ \Delta v \\ \Delta w \end{Bmatrix} = \frac{1}{t} \mathbf{N} \boldsymbol{\delta}_e \tag{5}$$

where the element strain matrix can be written as: $\mathbf{B} = \frac{1}{t}\mathbf{N}$.

The normal isotropic relationship of the contact element, taken from the Bandis hyperbolic model, is then given by:

$$k_{yy} = \frac{k_{yy0}}{\left(1 + \frac{v}{t}\right)^2} \tag{6}$$

with $k_{yy0} = \frac{E(1-\mu)}{(1+\mu)(1-2\mu)}$;

where k_{yy0} denotes the initial normal stiffness of the contact surface; E and μ represent elastic modulus and Poisson's ratio, respectively; v is the normal relative deformation, and t is the thickness of the contact surface.

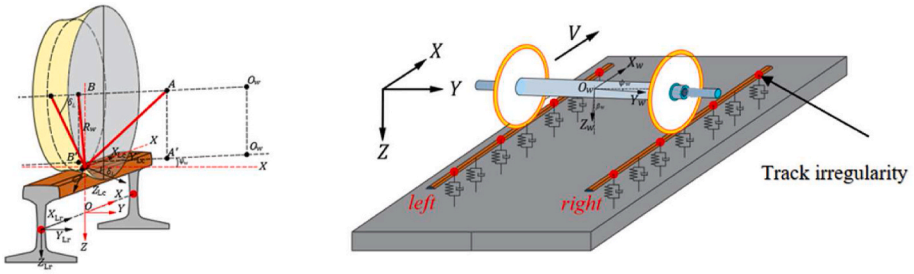

Fig. 5. Wheel-rail contact model.

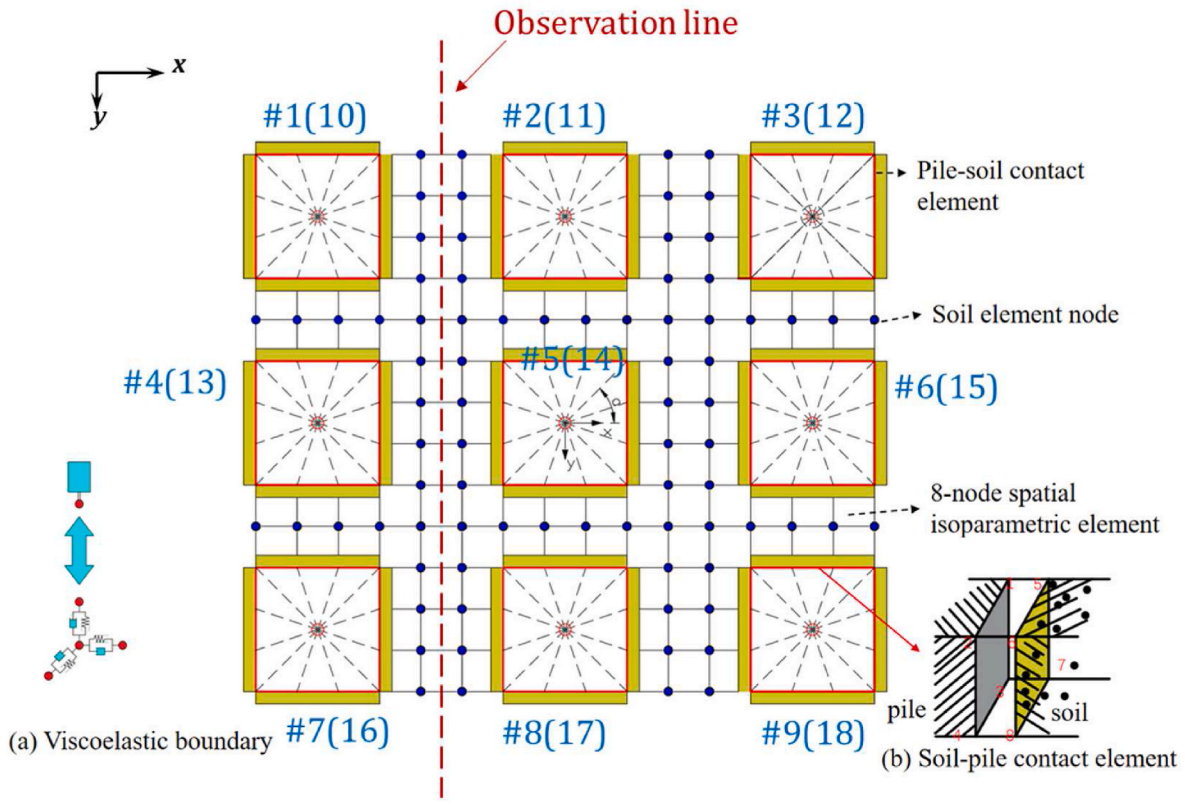

Fig. 6. Configuration for pile-soil coupling method.

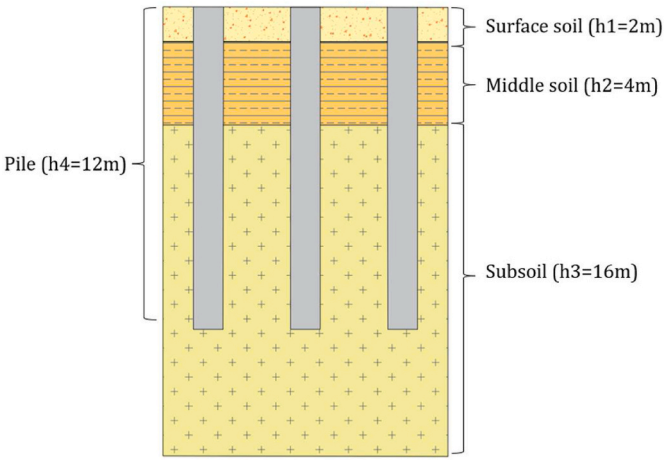

Fig. 7. Cross-section of layered soil.

The hyperbolic model [35] proposed by Clough was used to describe the contact surface tangential nonlinear stress-strain relationship. Assuming the terms in the contact surface are homogeneous, it can be formed as:

$$k_{xy} = k_{xy0}\left(1 - \frac{1}{\cos\alpha}\frac{r - \tau_{xy}}{(c - f\sigma_{yy})}\right) \tag{7}$$

$$k_{yz} = k_{yz0}\left(1 - \frac{1}{\cos\alpha}\frac{r - \tau_{yz}}{(c - f\sigma_{yy})}\right) \tag{8}$$

with

$$k_{xy0} = k_{zx0} = \frac{E\mu}{(1+\mu)(1-2\mu)}$$

where k_{xy0} and k_{yz0} are the initial tangential stiffness; c is the cohesion coefficient; f is the friction coefficient; α represents the frictional shear slip angle; r is the failure ratio. The asymptotic value of the hyperbola can be calculated by $(c - f\sigma_{yy})/r$, while the constitutive relation of the three-dimensional Desai thin layer element can be expressed in incremental form, given by:

$$\mathrm{d}\boldsymbol{\sigma} = \mathbf{D}\mathrm{d}\boldsymbol{\varepsilon} = \begin{bmatrix} k_{xy} & 0 & 0 \\ 0 & k_{yy} & 0 \\ 0 & 0 & k_{zx} \end{bmatrix} \begin{Bmatrix} d\varepsilon_{xy} \\ d\varepsilon_{yy} \\ d\varepsilon_{yz} \end{Bmatrix} \tag{9}$$

According to the principle of virtual work, the element stiffness matrix can be obtained:

$$\mathbf{K}^e = \boldsymbol{\delta}^T \int_{-1}^{1}\int_{-1}^{1} \mathbf{B}^{\mathrm{T}}\mathbf{D}\mathbf{B}|\mathbf{J}|dxdy \tag{10}$$

As discussed in Ref. [36], the application of the Desai thin layer element and its solution in the FE model is summarized as.

(1) The force **F** is divided into n parts ($n\Delta\mathbf{F}$) and then applied step by step;
(2) The stiffness matrices of the Desai elements are updated in the global stiffness matrix;
(3) The displacement increment and stress increment in the current step are calculated;
(4) According to **Eqs. 6-8**, the tangent stiffness of each direction of the pile-soil interface is obtained. Then the stiffness matrices of the Desai elements can be updated in the current incremental step;

(5) The next load increment $\Delta\mathbf{F}$ is applied and step (1) ~ (4) are repeated until $\mathbf{F}$ is completely applied.

2.5. Solution of the TTBPCPSI model

The coupling of the TTBI system and the PCPSI system is implemented considering equilibrium of bearing forces. The dynamic equations of motion of the TTBPCPSI system can be written as:

$$\begin{bmatrix} M_{VV} & 0 & 0 & 0 & 0 \\ 0 & M_{TT} & 0 & 0 & 0 \\ 0 & 0 & M_{BB} & 0 & 0 \\ 0 & 0 & 0 & M_{PP} & 0 \\ 0 & 0 & 0 & 0 & M_{SS} \end{bmatrix} \begin{Bmatrix} \ddot{X}_V \\ \ddot{X}_T \\ \ddot{X}_B \\ \ddot{X}_P \\ \ddot{X}_S \end{Bmatrix} + \cdots$$

$$\begin{bmatrix} C_{VV} & C_{VT} & 0 & 0 & 0 \\ C_{TV} & C_{TT} & C_{TB} & 0 & 0 \\ 0 & C_{BT} & C_{BB} & C_{BP} & 0 \\ 0 & 0 & C_{PB} & C_{PP} & C_{PS} \\ 0 & 0 & 0 & C_{SP} & C_{SS} \end{bmatrix} \begin{Bmatrix} \dot{X}_V \\ \dot{X}_T \\ \dot{X}_B \\ \dot{X}_P \\ \dot{X}_S \end{Bmatrix} + \cdots \tag{11}$$

$$\begin{bmatrix} K_{VV} & K_{VT} & 0 & 0 & 0 \\ K_{TV} & K_{TT} & K_{TB} & 0 & 0 \\ 0 & K_{BT} & K_{BB} & K_{BP} & 0 \\ 0 & 0 & K_{PB} & K_{PP} & K_{PS} \\ 0 & 0 & 0 & K_{SP} & K_{SS} \end{bmatrix} \begin{Bmatrix} X_V \\ X_T \\ X_B \\ X_P \\ X_S \end{Bmatrix} = \begin{Bmatrix} F_V \\ F_T \\ 0 \\ 0 \\ 0 \end{Bmatrix}$$

where the subscripts "B", "P", and "S" denote the bridge, pier-cap-pile, and soil, respectively.

The high DOF system is classified into two sub-systems: the train-track-bridge subsystem and the pier-cap-pile-soil subsystem. The dynamic equation of motion of the TTBPCPSI system can then be rewritten as:

$$\begin{cases} \begin{bmatrix} \mathbf{M}_{OO} & \mathbf{0} \\ \mathbf{0} & \mathbf{M}_{UU} \end{bmatrix} \begin{Bmatrix} \ddot{\mathbf{X}}_O \\ \ddot{\mathbf{X}}_U \end{Bmatrix} + \begin{bmatrix} \mathbf{C}_{OO} & \mathbf{0} \\ \mathbf{0} & \mathbf{C}_{UU} \end{bmatrix} \begin{Bmatrix} \dot{\mathbf{X}}_O \\ \dot{\mathbf{X}}_U \end{Bmatrix} + \cdots \\ \begin{bmatrix} \mathbf{K}_{OO} & \mathbf{0} \\ \mathbf{0} & \mathbf{K}_{UU} \end{bmatrix} \begin{Bmatrix} \mathbf{X}_O \\ \mathbf{X}_U \end{Bmatrix} = \begin{Bmatrix} \mathbf{F}_O \\ \mathbf{F}_U \end{Bmatrix} \\ \begin{Bmatrix} \mathbf{F}_O \\ \mathbf{F}_U \end{Bmatrix} = -\begin{Bmatrix} \mathbf{K}_{OU}\mathbf{X}_O \\ \mathbf{K}_{UO}\mathbf{X}_U \end{Bmatrix} - \begin{Bmatrix} \mathbf{C}_{OU}\dot{\mathbf{X}}_O \\ \mathbf{C}_{UO}\dot{\mathbf{X}}_U \end{Bmatrix} \end{cases} \tag{12}$$

where $\mathbf{F}$ denotes the force vector; $\ddot{\mathbf{X}}$, $\dot{\mathbf{X}}$ and $\mathbf{X}$ denote the acceleration, velocity, and displacement vectors, respectively; the subscripts "O" and "U" represent the superstructure and substructure respectively.

The multi-time-step method is then used to improve the solution efficiency. The multi-time-step size is $n\Delta t$, and the solution of superstructure and substructure can be written as:

$$Q_O^t\left(\ddot{\mathbf{X}}_O \quad \dot{\mathbf{X}}_O \quad \mathbf{X}_O\right) = \mathrm{I}\left(\mathbf{F}_O^t \quad \mathbf{M}_{OO}^t \quad \mathbf{C}_{OO}^t \quad \mathbf{K}_{OO}^t \quad Q_O^{t-\Delta t} \quad Q_U^{t-\Delta t}\right) \tag{13}$$

$$\begin{cases} Q_U^t = I\left(F_U^{t-n\Delta t} \quad \mathbf{M}_{UU}^t \quad \mathbf{C}_{UU}^t \quad \mathbf{K}_{UU}^t \quad Q_O^{t-n\Delta t} \quad Q_U^{t-n\Delta t}\right) \quad \text{For } \psi = 0; \\ Q_U^t = Q_U^{t-\psi} + \psi\dfrac{Q_U^{t-\psi+n} - Q_U^{t-\psi}}{n} \quad \text{For } \psi \neq 0; \end{cases} \tag{14}$$

with

$$\mathbf{F}_O^{t-\Delta t} = \mathbf{F}^{t-\Delta t} - \left(\mathbf{K}_U^{t-\Delta t}\mathbf{X}_U^{t-\Delta t} - \mathbf{C}_U^t\dot{\mathbf{X}}_U^{t-\Delta t}\right),$$

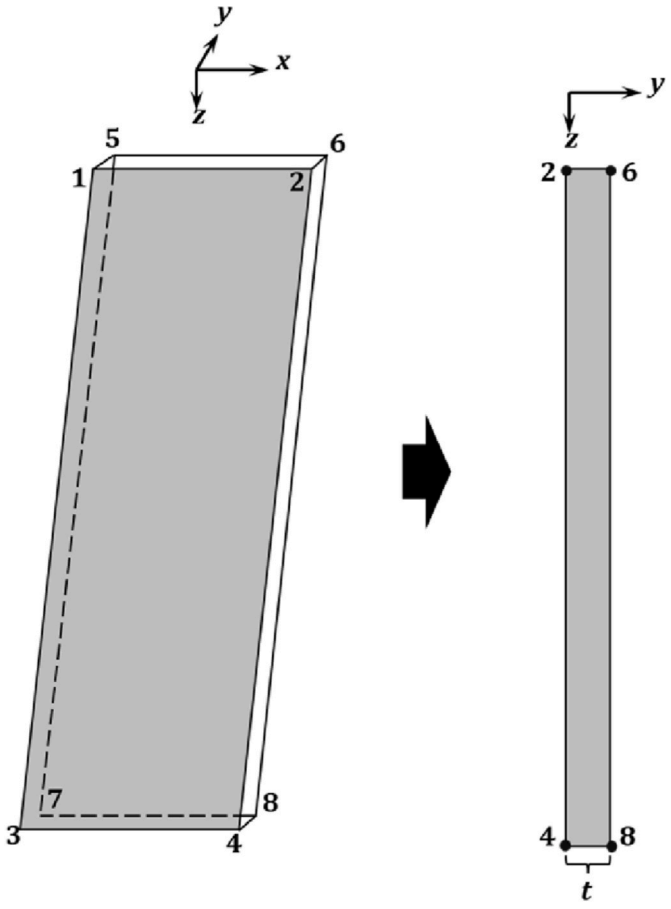

Fig. 8. Schematic of the Desai element.

$$\mathbf{F}_U^{t-\Delta t} = \mathbf{F}^{t-\Delta t} - \left(\mathbf{K}_O^{t-\Delta t}\mathbf{X}_O^{t-\Delta t} - \mathbf{C}_O^t\dot{\mathbf{X}}_O^{t-\Delta t}\right),$$

where Q_O^t and Q_U^t represent the solution of the superstructure and substructure at a given timestep respectively, while Δt denotes the time-step size. I is the symbol of implicit integration and ψ represents the interpolation multiple for the non-integration time points. More detailed information about the multi-time-step method can be found in Refs. [37, 38].

3. Model validation

The TTBI model has been validated in previous work [39], meaning the emphasis of this section is put on the validation of the piled foundations model. As shown in Fig. 9, to validate the practicality and effectiveness of the present piled foundations model, an equivalent FE model is constructed using the commercial software, ABAQUS. A harmonic load in the vertical direction with an amplitude of 10 kN and a frequency of 20 Hz is applied to pile #5. Fig. 10 displays a comparison of the responses calculated by the proposed model and the ABAQUS model, where the displacements are recorded at pile #5, and the observation position of ground is at the center of piles #4 and #5. It can be seen that the responses calculated by the proposed model agree well with that of the ABAQUS model, reflecting the effectiveness of the proposed approach. Due to the coulomb friction contact model applied in ABAQUS, there is a significant difference in the extreme values of the displacement curves for the pile and ground. The limitation of the friction contact model is that the influence of constitutive changes of two objects on contact behavior is not considered. Thus the Desai contact element is applied because it is closer to the physical situation. It can be seen that a transient vibration exists in the time domain and under the

soft soil condition, the special frequency of the transient vibration is close to 1.2 Hz. This shows that the dynamic response of the pile-soil interaction will be excited by low-frequency excitation, and its main influence on the TTBI system will be in the low-frequency range.

4. Numerical studies

In this section, to demonstrate the coupled vibration properties of the TTBI and the piled foundations in soft soil, two illustrative examples are implemented. The first example compares the response of the TTBPCPSI system and the TTBI system. The second example investigates the dynamic behavior of pile-soil interaction subject to different train speeds. The soil-pile interaction system is located at piers #7 and #8.

4.1. Example 1: the comparison of the responses of TTBPCPSI and TTBI

In this subsection, the responses of the TTBPCPSI and TTBI models are compared. They are solved using the *Newmark-β* integral method with a time step size Δt of 0.0001 s, while the multi-time step size $n\Delta t$ for solving the PCPSI system is 0.0003 s. The excitation of the dynamic system, i.e., the track irregularity, is converted using the Fourier transform method applied to the Chinese HSR spectrum [40] (1–50 m wavelength) and the Sato spectrum [41] (0.05–1 m wavelength). The time history of the track irregularity is displayed in Fig. 11. The train speed is 300 km per hour.

4.1.1. Response of the train system

Fig. 12 compares the vertical accelerations of the motor car body calculated using both models. The discrepancy between accelerations is amplified when the train passes over the girders due to the influence of piled foundations. This difference can be observed in the time domain due to the large displacement of the pile buried in the soft soil, shown by the pile displacements in Fig. 13. The power spectrum density (PSD) can give a better view of the influence of the pile-soil system, as shown in Fig. 12(b). The PSDs are estimated using the Pwelch method with a window 20 m in length. The natural frequencies of the car body vertical motion and bogie vertical motion are 0.84 and 0.98 Hz, respectively. It can be seen from the PSD curve that the car body vertical vibration in the frequency band below 7 Hz is excited. On one hand, this frequency band includes the two natural frequencies of the vehicle and the long wavelength components of the track irregularity, while on the other hand, the displacement of the pile provides additional low-frequency excitation for the TTBI system (Fig. 13). The enlarged frequency band can be seen in the PSD curve. The short-wavelength irregularity has a small effect on the car body vibrations because the rigid vehicle is a low-frequency system while the highest excited frequency is near 40 Hz. This specific frequency is caused by the nonlinear Hertz contact spring [42].

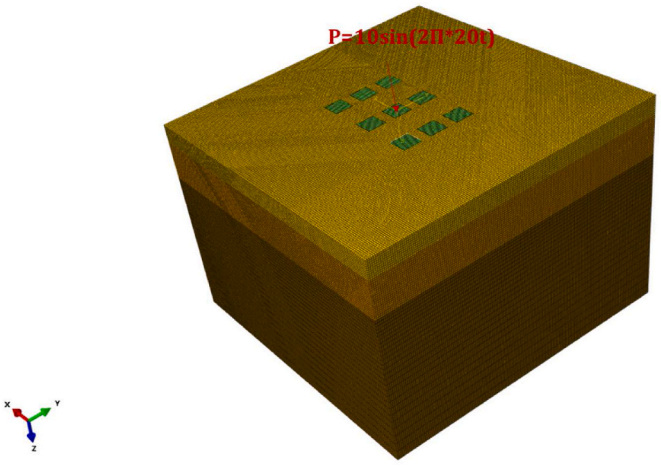

Fig. 9. Pile-soil interaction model established in ABAQUS.

The vertical wheel-rail force calculated by the two models is shown in Fig. 14. It can be observed that the specific frequency of Hertz contact stiffness is near 37 Hz. The track irregularities generated by the China's HSR spectrum and the Sato spectrum are discontinuous at 83.3Hz. Therefore, an abrupt change of wheel-rail forces is observed at this frequency. This special frequency can be calculated by

$$\Omega = V_t/\lambda \tag{15}$$

where $V_t = 300$ km/h denotes the train speed, $\lambda = 1$ m denotes the boundary wavelength of the track irregularities generated by two types of spectrums. It can be seen that the piled embedded in soft soil does not affect the wheel-rail forces strongly. It is track irregularities that affects the dynamic behavior of the wheel-rail interaction system rather than the mechanics properties of the substructure. The similar conclusion can be found in our previous works [43–45].

4.1.2. Response of the track-bridge system

The response of two observation points located in the mid-span of the 7th girder (above the pile-soil system in the TTBPCPSI model, denoted as ##1) and the mid-span of the 5th girder (denoted as ##2), are compared. Fig. 15 shows the rail displacements recorded at the two observation points. It can be seen that when the train passes through ##1, the large displacement of the pile is transferred to the rail, and the rail displacements sharply increase. In contrast, the responses observed at point ##2 have a reduced difference between each other, indicating the piled foundations have limited influence on the other span. This can be also seen in Fig. 15(b) because when the train is far away from point ##2, the displacement calculated by the TTBPCPSI model only shows a minimal increase compared to that of the TTBI model.

As shown in Fig. 15(a), there are two points of particular interest: A1 and A2. A1 is the 1st wheelset of the vehicle passing onto the 7th girder and A2 is the 4th wheelset of the last trailer passing over the 7th girder. It can be seen that when the train leaves the 7th span, the rail displacement does not immediately decrease, but instead slowly decreases and a small upward arch appears. This response is similar to the displacement of the track-simply-supported beam bridge system, as shown in Fig. 15(b) (120–250 m).

A simplified method to evaluate the effect of pile displacement on mid-span displacement is the rigid displacement method, as shown in Fig. 16. Assuming the girder is a rigid body, the mid-span displacement can be approximated by:

$$\widetilde{U}_B^m(t) \approx \frac{\sum_{i=1\sim N} U_{P,i}(t)}{2N} \tag{16}$$

where $\widetilde{U}_B^m$ denotes the rigid displacement of the mid-span under the pile displacement; N is the number of piles, and $U_{P,i}(t)$ is the time history of the i-th pile.

Fig. 17 displays the mid-span displacement of the two observation points. It can be seen that the overall trend of the mid-span displacement curve estimated by the rigid displacement method is close to that predicted by the TTBPCPSI model, and the difference between the two curves reflects the influence of the train load. Fig. 17(a) shows the displacement difference between the TTBPCPSI model and the rigid model, and the results calculated using the TTBI model. It can be seen that using the rigid displacement method to predict the mid-span displacement gives a larger result than using the flexible model, which also shows the importance of considering piled foundations in the TTBI system. Fig. 17(b) shows the mid-span displacement has similar behavior to the rail displacement.

4.1.3. Vibration transmission characteristics

To estimate the vibration transmission of the dynamic interaction system, the power flow method is used. Power flow reflects the energy transmission through the interaction of two structures, and is calculated

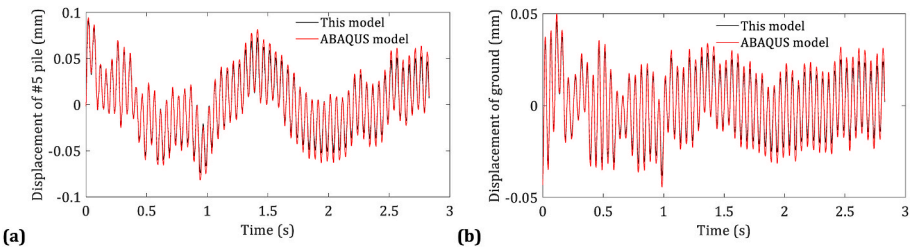

Fig. 10. Comparison of responses (a. pile displacement; b, ground displacement).

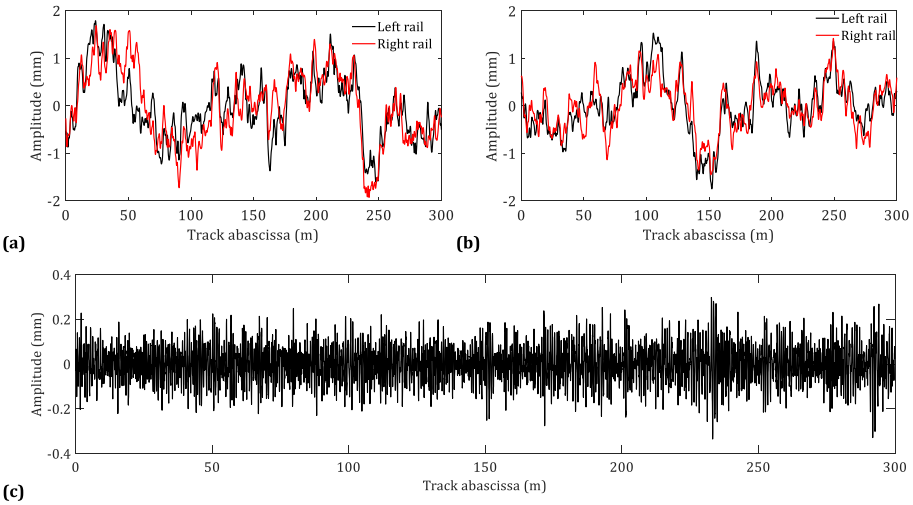

Fig. 11. Time history of track irregularity excitations (a. mid-long wavelength components for vertical direction; b. mid-long wavelength components for lateral direction; c. short wavelength components for both vertical and lateral directions).

as [46]:

$$P=\frac{1}{T}\int_0^T F(t)\dot{U}(t)dt \tag{17}$$

where P is the mean power in one period T; F and $\dot{U}$ represent the interaction force and the velocity of the structure.

Using the Fourier transform, the power flow in the frequency domain is estimated by:

$$P(\Omega)=\frac{1}{2}\mathrm{Re}[F(\Omega)\dot{U}^{*}(\Omega)] \tag{18}$$

where the superscript "*" is the conjugation operator.

Figs. 18 and 19 display the results of the power flow of the TTBPCPSI and the TTBI systems for the track slab, base plate, and bridge. It can be seen from the results that the energy transmitted to the structure increases significantly at low-frequencies due to the influence of the pile-soil substructure. Power flow can reach 1e6 J/s in the frequency band 0–1 Hz, while for the other 3 cases, the power flow is in the range 1e3~1e4 J/s. It can also be seen from Figs. 13, **15**, and **17** that the dominant frequency of the pile vertical motion is close to 1.2 Hz, which demonstrates that the energy at this frequency will increase.

4.2. Example 2: dynamic behavior of the pile-soil interaction system

In this subsection, three train speeds: 300, 350 km/h and 400 km/h, are selected to study the influence of train speed on the dynamic behavior of the pile-soil interaction system. The track irregularity excitation is the same as in Example 1.

4.2.1. With respect to pile vibration

Figs. 20 and 21 display the vertical accelerations of piles #5 and

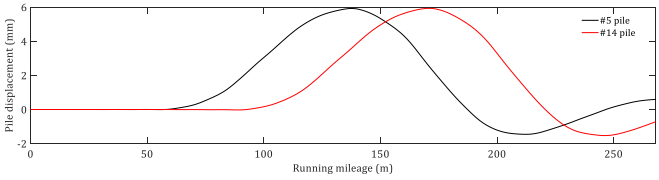

Fig. 13. Vertical displacement of piles #5 and #14.

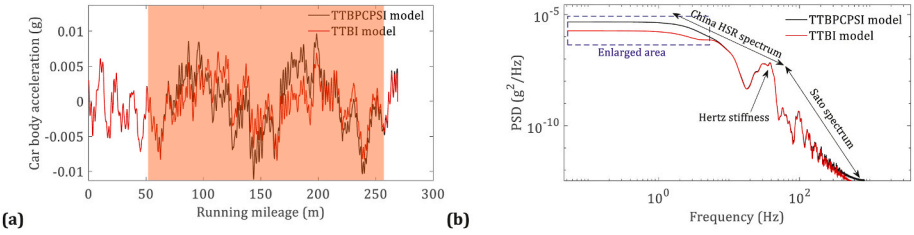

Fig. 12. Comparison of car body vertical acceleration (a. time history; b. PSD curve).

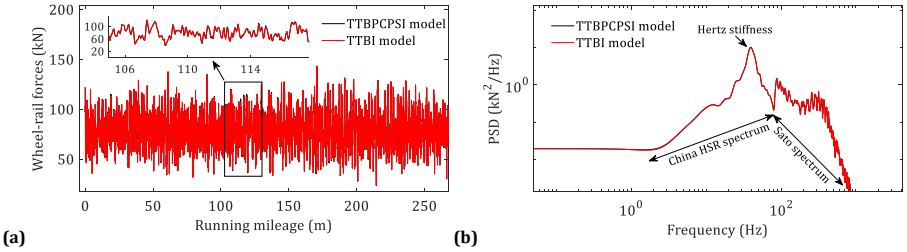

Fig. 14. Comparison of wheel-rail vertical forces (a. time history; b. PSD curve).

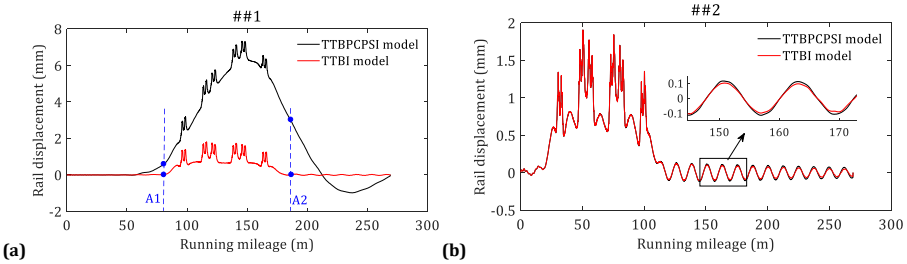

Fig. 15. Comparison of rail vertical displacement (a. for ##1; b. for ##2).

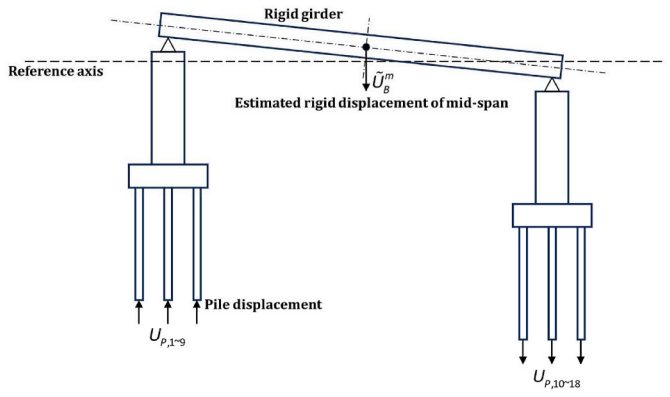

Fig. 16. Schematic of the rigid displacement of mid-span under pile displacement.

#14. It can be observed from the results that four special frequencies are excited. The first frequency, Ω_v, is excited by the train axle loads. The frequency range of Ω_v can be estimated by Ref. [47]:

$$\Omega_v \in \left(\frac{V_T}{2L_w + 2L_b}, \quad \frac{V_T}{2L_b} \right) \tag{19}$$

where V_T denotes the train speed; L_b denotes the half-distance between the front and rear bogies; L_w denotes the half-distance between the front and rear wheelsets.

It can be seen from the results that the pile vibration induced by the train load increases when the speed reaches 400 km/h, indicating the effect of train speed on the HSR bridge should be considered during design. The second frequency of interest is close to the specific frequency induced by the Hertz contact stiffness, demonstrating the vibrations produced by the wheel-rail impact can transfer to the pile. Therefore the excitation of the wheel-rail interaction system from track irregularities is a factor that should be considered when analyzing the vibration of pile-soil interaction. The last two frequencies of interest, Ω_1 and Ω_2, are close to the first and second natural frequencies of the pile vertical vibration: 84.3 and 173.2 Hz. It can be seen that the vibration amplitudes at these latter three frequencies are not at their maximum for the 400 km/h case.

The complex TTBPCPSI system shows uncertainty regarding correlation with train speed, which can be found in the rail displacements under the 1st wheelset of the locomotive and the 4th wheelset of the 2nd trailer, as shown in Fig. 22. The rail displacements under the 1st wheelset of the driving car are largest when the train speed is 250 km/h, while the displacements under the 4th wheelset of the 2nd trailer are largest when the train speed is 400 km/h. This demonstrates that the under-rail structures are sensitive to the train speed, especially for the pile displacement response, which has a time delay as shown in Fig. 23. The time delay of the substructure displacement changes the contact behavior of wheel-rail interaction, meaning different exciting wheel-rail behavior influences the vibration characteristics of the substructure. The analogous uncertainty of responses can also be found in the rotation behavior of the side pile.

Moreover, the rotation of the piles is also an important index for investigating their dynamic behavior. It reflects their lateral vibration

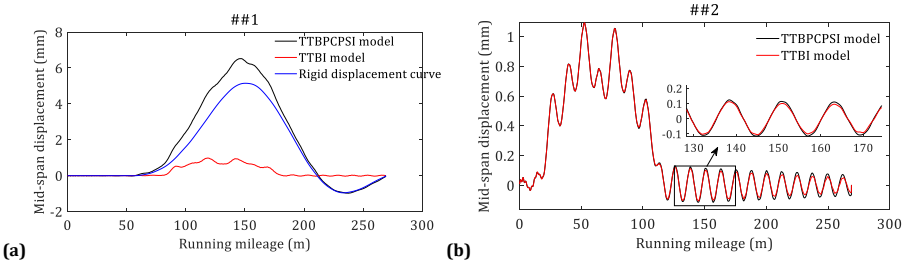

Fig. 17. Comparison of mid-span vertical displacement (a. for ##1; b. for ##2).

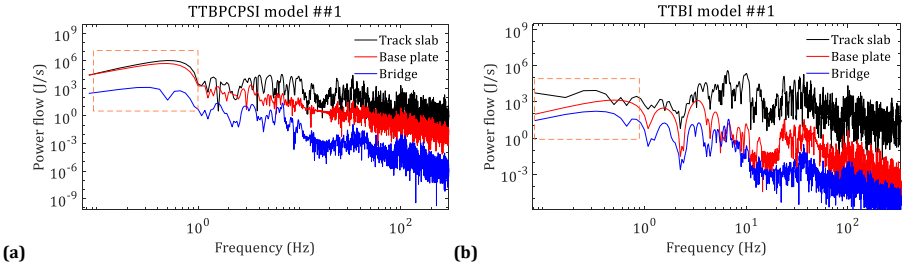

Fig. 18. Comparison of frequency-domain power flow at observation point ##1 (a. TTBPCPSI model; b. TTBI model).

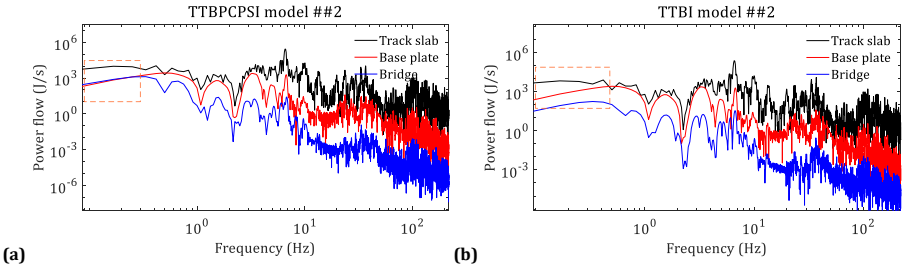

Fig. 19. Comparison of power flow at observation point ##2 (a. TTBPCPSI model; b. TTBI model).

subject to train excitation. In Fig. 24, the maximum rotations of the side piles are displayed. The higher train speed does not produce greater pile rotation, as shown for piles #2, 3, 8, and 9, at train speed 250–350 km/h. This shows the relationship between the lateral vibration caused by the train and the train speed is not linear. When the train speed reaches 400 km/h, pile rotation is at a maximum. The maximum rotation is 2.408 rad for pile #8 when the train speed is 400 km/h. Pile #2 and 8 have greater rotation values than the other piles, which indicates that the lateral vibrations of the pile in the middle have a higher vibration level.

4.2.2. *With respect to the soil vibration*

The observation line (as shown in Fig. 6) between the first and second rows of piles is used to record the vibration time history of the soil. The accelerations recorded from the observation line are shown in Fig. 25. There are three stages that can be found in the acceleration contour: positive values (when the train enters the pile-soil area), negative values (when the train runs in the pile-soil area), and positive values (when the train completely runs off the pile-soil area). The maximum amplitude of the acceleration along the observation line shows a correlation with the train speed. For example, when the train speed is 250 km/h, it can be seen that the acceleration is in the range of 0.08–0.08 m/s^2, while it increases to −0.2~0.2 m/s^2 once the train speed reaches 400 km/h.

Vibration acceleration level (VAL) is now used to study the ground vibration (international *Standard ISO2631*) at three soil observation points. The first and second points are 1 m away from piles #5 and #14, and the third point is located in the center between the first and second points. The VALs of the three observation points are displayed in Fig. 26. It can be seen that there are two dominant frequency ranges: 4–10 Hz and 25–40 Hz. The first frequency range is close to the special frequency Ω_v induced by the train axle spacing, while the second dominant

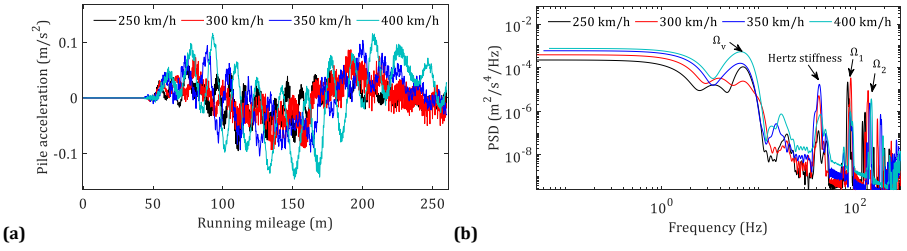

Fig. 20. Comparison of pile acceleration at observation point #5 (a. time history; b. PSD curve).

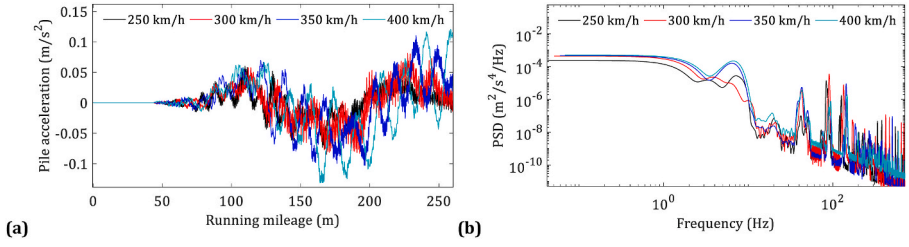

Fig. 21. Comparison of pile acceleration at observation point #14 (a. time history; b. PSD curve).

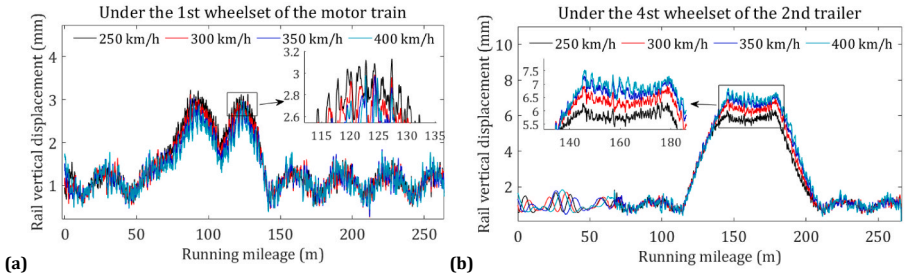

Fig. 22. Rail vertical displacements (a. under the 1st wheelset of the motor train; b. under the 4th wheelset of the 2nd trailer).

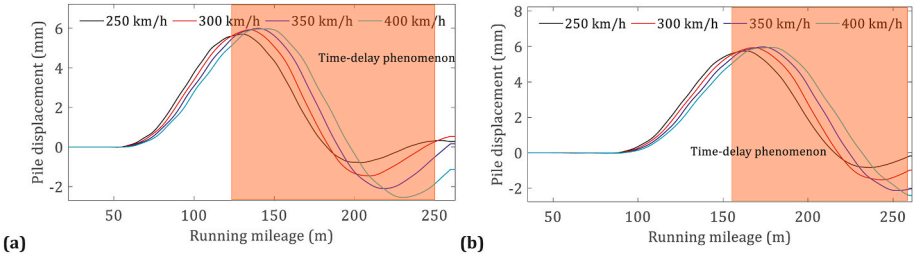

Fig. 23. Pile displacements subjected to the different train speeds (a. #5 pile; b. #14 pile).

frequency is close to the frequency of the Hertz contact stiffness, which is amplified by the excitation due to track irregularities. The train speed is also an important factor that influences the amplitude of VALs. When the train speed reaches 400 km/h, the overall level of VALs is greater than the other speed cases. Compared with the dominant frequency of the Hertz contact stiffness, the short-wavelength track irregularity has no obvious effect on the high-frequency vibration of the ground. The simulation results demonstrate that train speed and the wheel-rail interaction are the most important factors that dominate vibration generation.

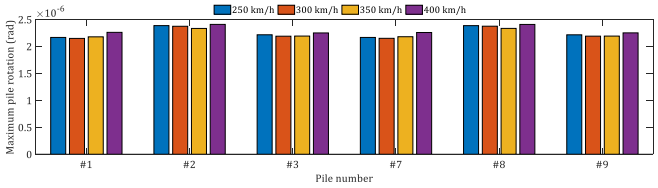

Fig. 24. Maximum pile rotation subjected to different train speeds.

5. Concluding remarks

In this study, a numerical model is developed to investigate the dynamic performance of TTBI considering piled foundations in soft soil. It is formed from two sub-models: a TTBI sub-model and a PCPSI sub-model. The two sub-models are coupled and solved through the equilibrium of bearing forces. Track irregularities are considered as the system excitation and Desai elements are used to simulate pile-soil contact behavior. The pile-soil model is validated, and conclusions are drawn from the numerical analysis.

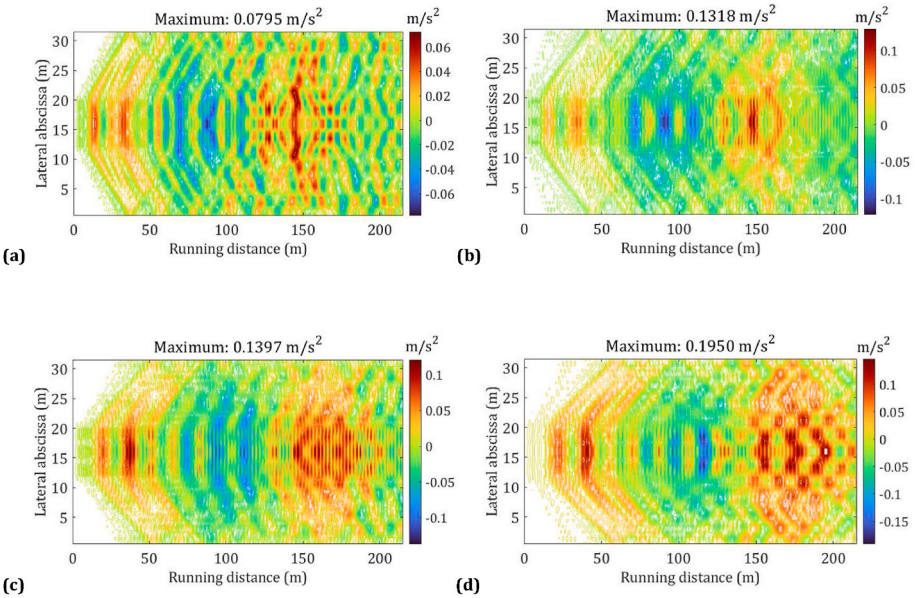

Fig. 25. Soil accelerations recorded from the observation line (a. 250 km/h; b. 300 km/h; c. 350 km/h; d. 400 km/h).

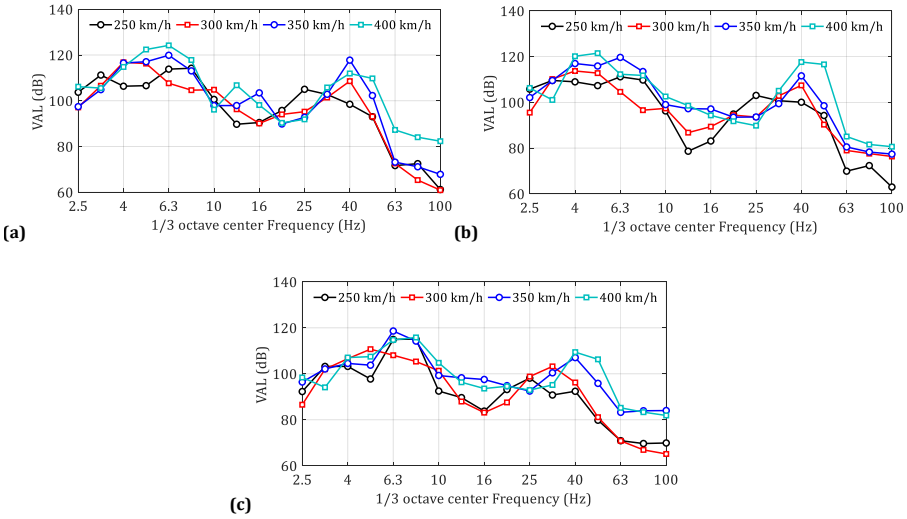

Fig. 26. Comparison of VALs calculated at different locations (a. first point; b. second point; c. third point).

(1) The transient vibration of pile-soil interaction can be observed under harmonic loads, in which the dominant frequency of the pile-soil system is close to 1.2 Hz, affecting the low frequency vibration of the TTBI system. Comparing the power flow of the TTBPCPSI and the TTBI systems at low frequencies, the maximum value of the power flow increases from 1e4 J/s to 1e6 J/s, and an increase in the low-frequency vibration of the train, track and bridge is also observed.
(2) Regarding wheel-rail forces, foundation type has no obvious effect on the simulation results. This shows that wheel-rail interaction is dominated by track irregularities rather than the response of the piles embedded in soft soil. Thus, when studying only the dynamic behavior of wheel-rail interaction, the substructure can be simplified.
(3) The displacements of two adjacent piled foundations are time-delayed due to the moving train, which makes it challenging to study the influence of train speed on the dynamic system. However, for the system studied, the following was found: The rail displacements observed at the point under the first driving car wheelset decreased with increasing train speed. In contrast, it grew with increasing train speed considering the fourth wheelset of the trailer. For the pile and soil, higher train speeds resulted in increased accelerations.
(4) In the presence of soft soils, vibrations at the piles' dominant frequencies were not transmitted into the surrounding soil - VALs showed that the vibration at these frequencies was not excited. Therefore, although soft soil has a vibration isolation effect on the high-frequency vibrations transmitted from the piles, its low stiffness characteristics cause larger displacement and other adverse effects.

CRediT authorship contribution statement

Borong Peng: Writing – original draft, Software, Formal analysis. **Lei Xu:** Writing – review & editing, Funding acquisition. **David P. Connolly:** Writing – review & editing, Validation. **Zheng Li:** Writing – review & editing, Investigation, Conceptualization. **Xuhui He:** Funding acquisition. **Yuanjie Xiao:** Investigation. **Yunlong Guo:** Writing – review & editing, Methodology.

Declaration of competing interest

The authors declare that they have no known competing financial interests or personal relationships that could have appeared to influence the work reported in this paper.

Data availability

The data that has been used is confidential.

Acknowledgments

This work was supported by the National Natural Science Foundation of China (Grant Nos. 52327810; 52378468; 52008404; U1734208).

Appendix

Table 1
Vehicle parameters

Parameters (Unit)	Value
Car body mass (kg)	48000
Bogie mass (kg)	3200
Wheelset mass (kg)	2400
Mass moment of inertia of car body about *X*-axis (kg·m^2)	115000
Mass moment of inertia of car body about *Y*-axis (kg·m^2)	2300000
Mass moment of inertia of car body about *Z*-axis (kg·m^2)	2300000
Mass moment of inertia of bogie about *X*-axis (kg·m^2)	3200
Mass moment of inertia of bogie about *Y*-axis (kg·m^2)	7200

(*continued on next page*)

Table 1 (*continued*)

Parameters (Unit)	Value
Mass moment of inertia of bogie about *Z*-axis (kg·m^2)	6800
Mass moment of inertia of wheelset about *X*-axis (kg·m^2)	1200
Mass moment of inertia of wheelset about *Y*-axis (kg·m^2)	200
Mass moment of inertia of wheelset about *Z*-axis (kg·m^2)	1200
Stiffness coefficient of primary suspension along *X*-axis (MN/m)	9
Stiffness coefficient of primary suspension along *Y*-axis (MN/m)	3
Stiffness coefficient of primary suspension along *Z*-axis (MN/m)	1.04
Stiffness coefficient of secondary suspension along *X*-axis (MN/m)	0.24
Stiffness coefficient of secondary suspension along *Y*-axis (MN/m)	0.24
Stiffness coefficient of secondary suspension along *Z*-axis (MN/m)	0.4
Damping coefficient of primary suspension along *Z*-axis (kN·s/m)	45
Damping coefficient of secondary suspension along *Y*-axis (kN·s/m)	3
Damping coefficient of secondary suspension along *Z*-axis (kN·s/m)	98
Semi-longitudinal distance between bogies (m)	7.85
Semi-longitudinal distance between wheelsets in bogie (m)	1.25
Wheel radius (m)	0.46

Table 2
Tack parameters

Parameters (Unit)	Value
Elastic modulus of the rail (N/m^2)	2.059×10^{11}
Torsional inertia of the rail (m^4)	3.741×10^{-5}
Rail second moment of area about the *Y*-axis (m^4)	3.217×10^{-5}
Rail second moment of area about the *Z*-axis (m^4)	5.24×10^{-6}
Rail torsional stiffness coefficient (N·m/rad)	1.958×10^5
Rail mass per unit length (kg/m)	60.64
Fastener spacing (m)	0.63
Track slab size (m·m·m)	$5.6 \times 2.5 \times 0.21$
Concrete grade for track slab	C60
Longitudinal characteristics for slab	Unit
Filling layer thickness (m)	0.09
Elasticity modulus of filling layer (MPa)	3.25×10^4
Base plate size (m·m)	3.1×0.3
Concrete grade for track base plate	C40

Table 3
Main parameters of the bridge

Parameters (Unit)	Value
Elastic modulus (pa)	3.55×10^{10}
Poisson's ratio	0.2
Density (kg /m^3)	2500
Area of mid-span (m^2)	47.8128
Area of beam-end (m^2)	69.2528
Inertia moment of the mid-span cross section about X axis (m^4)	22.984
Inertia moment of the mid-span cross section about Y axis (m^4)	13.088
Inertia moment of the mid-span cross section about Z axis (m^4)	86.951
Inertia moment of the beam-end cross section about X axis (m^4)	35.435
Inertia moment of the beam-end cross section about Y axis (m^4)	18.791
Inertia moment of the beam-end cross section about Z axis (m^4)	105.667

Table 4
Spring and damping parameters

Parameters (Unit)	Value
Lateral stiffness of discrete spring reflecting property of fastener (N /m)	3.0×10^7
Vertical stiffness of discrete spring reflecting property of fastener (N /m)	5.0×10^7
Lateral damping coefficient of discrete damper reflecting property of fastener (N ·s/m)	3.0×10^4
Vertical damping coefficient of discrete damper reflecting property of fastener (N ·s/m)	3.6×10^4
Lateral stiffness of continuous spring reflecting property of CAM per unit length (N/m^2)	1.5×10^9
Vertical stiffness of continuous spring reflecting property of CAM per unit length (N/m^2)	1.5×10^9
Lateral damping coefficient of continuous damper reflecting property of CAM per unit length (N ·s/m^2)	8.3×10^4
Vertical damping coefficient of continuous damper reflecting property of CAM per unit length (N ·s/m^2)	8.3×10^4

(*continued on next page*)

Table 4 (*continued*)

Parameters (Unit)	Value
Lateral spring stiffness reflecting property of foundation of pier (N /*m*)	6.0×10^8
Vertical spring stiffness reflecting property of foundation of pier (N /*m*)	6.0×10^9
Lateral damping coefficient reflecting property of foundation of pier (N /*m*)	0
Lateral damping coefficient reflecting property of foundation of pier (N /*m*)	0

Table 5
Main parameters of the pile-soil interaction model

Item	Surface soil	Middle soil	Subsoil	pile
Elastic modulus (MPa)	4×10^6	5×10^6	6×10^6	1×10^{11}
Gravity (kN/m^3)	18	19	15	25
Poisson's ratio	0.35	0.25	0.25	0.2
Friction angle	5	30	30	/
Cohesion (kPa)	20	15	10	/
Thickness (m)	2	4	16	12

Table 6
The size of the substructure

Item	Value
Radius of pier (m)	$3.3 \sim 4$
Cap size (m·m·m)	$9 \times 15 \times 2.5$
Pile size (m·m·m)	$5 \times 3 \times 12$

References

[1] Zhai WM, Han ZL, Chen ZW, et al. Train–track–bridge dynamic interaction: a state-of-the-art review. Veh Syst Dyn 2019;57(7):984–1027.
[2] He XH, Wu T, Zou YF, et al. Recent development of high-speed railway bridges in China. Struct Infrastruct Eng 2017;13:1584–95.
[3] Matsuura Akio. Study on train safety of long suspension bridge. Japan Railway Technology Association 1988;31(5):12–4.
[4] Matsuura Akio. High-speed rail vehicles interact with Bridges. Railway Technology Research Data 1974;31(5):14–7.
[5] Matsuura Akio. Vertical allowable disturbance of Shinkansen railway bridge. Railway Technol Res Report 1974;31(10):445–9.
[6] Tanabe M, Yamada Y. Model method for interaction of train and bridge. J Comput Struct 1987;27(1):119–227.
[7] Li XZ, He HA, Wang M, et al. Influence of long-span bridge deformation on driving quality of high-speed trains. Int J Rail Transp 2023:2324–8378.
[8] Zeng Q, Stoura CD, Dimitrakopoulos EG. A localized Lagrange multipliers approach for the problem of vehicle-bridge-interaction. Eng Struct 2018;168:82–90.
[9] Azimi H, Galal K, Pekau OA. A modified numerical VBI element for vehicles with constant velocity including road irregularities. Eng Struct 2011;33:2212–20.
[10] Xin LF, Mu D, Choi DH, et al. General conditions for the resonance and cancellation of railway bridges under moving train loads. Mech Syst Signal Process 2023;183:109589.
[11] Guo W, He XE, Jiang LZ, et al. The effect of high-speed railway train on the seismic response of bridge under earthquakes. Eng Struct 2024;303:117446.
[12] Gou HY, Chen XY, Bao Y, et al. A wind hazard warning system for safe and efficient operation of high-speed trains. Autom ConStruct 2021;132:103952.
[13] Wang KW. Wheel contact point trace line and wheel/rail contact geometry parameters computation. J Southwest Jiaot Univ 1984;1:89–99.
[14] Chen G, Zhai WM. A new wheel/rail spatially dynamic coupling model and its verification. Veh Syst Dyn 2004;41(4):301–22.
[15] Luo J, Zhu SY, Zhai WM. An advanced train-slab track spatially coupled dynamics model: theoretical methodologies and numerical applications. J Sound Vib 2021;501(9):116059.
[16] Yang JJ, Zhu SY, Zhai WM. Prediction and mitigation of train-induced vibrations of large-scale building constructed on subway tunnel. Sci Total Environ 2019;668:485–99.
[17] Qu CZ, Tan XY, Xiao YJ, et al. Subgrade vibrations and long-term stability of an embankment-bridge transition zone in non-ballasted high-speed railway. Transp Geotech 2024;45:101199.
[18] Wu Y, Shi CG, Yu YH, et al. Dynamic behavior of precast epoxy asphalt track bed for transition zone in high-speed railway: a numerical approach. Transp Geotech 2023;40:100960.
[19] Zhang XY, Yu SS, Wang WP, et al. Nonlinear seismic response of the bridge pile foundation with elevated and embedded caps in frozen soils. Soil Dynam Earthq Eng 2022;161:107403.
[20] Chen Y, Lv Y, Wu K, et al. Numerical analysis of bridge piers under earthquakes considering pile-soil interactions and water-pier interactions. Ocean Eng 2019;266:113023.
[21] Li XZ, Zhang ZJ, Zhang X. Using elastic bridge bearings to reduce train-induced ground vibrations: an experimental and numerical study. Soil Dynam Earthq Eng 2016;85:78–90.
[22] Zhang ZJ, Li XZ, Zhang X, et al. Semi-analytical simulation for ground-borne vibration caused by rail traffic on viaducts: vibration-isolating effects of multi-layered elastic supports. J Sound Vib 2022;516:116450.
[23] Shan DS, Li Q. Coupled vibration analysis of railway curved girder bridge and vehicles with soil-structure interaction. J Chongqing Jianzhu Univ 2004;23(6):10–4 (in Chinese).
[24] Liang AT, Wang SB, Li LA, et al. Study on influence of soil-pile nonlinear interaction on vehicle-bridge coupling vibration. Eng Mech 2014;31:12. in Chinese.
[25] Romero A, Solís M, Domínguez J, et al. Soil–structure interaction in resonant railway bridges. Soil Dynam Earthq Eng 2013;47(23):108–16.
[26] Galvín P, Romero A, Moliner E, et al. Fast simulation of railway bridge dynamics accounting for soil–structure interaction. Bull Earthq Eng 2022;20(7):3195–213.
[27] Shamsi MG, Ghanbari A. Nonlinear dynamic analysis of qom monorail bridge considering soil-pile-bridge-train interaction. Transp Geotech 2020;22:100309.
[28] Xu L, Li Z, Bai W, et al. Numerical simulation platform for slab track systems subjected to a moving vehicle. Adv Eng Software 2021;154:102984.
[29] Zhai WM. Vehicle-track coupled dynamics. 4th. Beijing: Science Press; 2015.
[30] Goodman RE, Taylor RL, Brekke TL, et al. A model for mechanics of jointed rock. J Soil Mech Found Div 1968;94(3):637–60.
[31] Desai CS, Zaman MM, LightnerJ G, et al. Thin-layer element for interfaces and joints. Int J Numer Anal Met 1984;8(1):19–43.
[32] Xu L, Zhai WM. A three-dimensional model for train-track-bridge dynamic interactions with hypothesis of wheel-rail rigid contact. Mech Syst Signal Process 2019;132:471–89.
[33] Xu L, Yu ZW, Shi C, et al. A matrix coupled model for vehicle-slab track-subgrade interactions at 3-D space. Soil Dynam Earthq Eng 2020;128:105894.
[34] Andrew JD, Mark FR. Axisymmetric time-domain transmitting boundaries. J Eng Mech 1994;120(1):25–42.
[35] Clough GW, Duncan JM. Finite element analysis of retaining wall behavior. J Soil Mech Found Div 1973;99(4):1657–72.
[36] Ren QW, Shen L. Nonlinear finite element method and programming tutorial. Nanjing: Hohai University Press; 2021.
[37] Xu L, Zhai WM, Zhu SY, et al. An efficient method for train–track–substructure dynamic interaction analysis by implicit-explicit integration and multi-time-step solution. Railw Eng Sci. 2023;31:20–36.

[38] Li Z, Xu L, Liu PF, et al. Numerical modeling and analysis for nonlinear stiffness of subgrade soil subject to 3-D vehicle-track interaction. Transp Geotech 2023;42(1):101095.
[39] Xu L, Zhai WM, Li ZL. A coupled model for train-track-bridge stochastic analysis with consideration of spatial variation and temporal evolution. Appl Math Model 2018;63:709–31.
[40] PSD of ballastless track irregularities of high-speed railway. Beijing: China Railway Press; 2014.
[41] Sato Y. Study on high-frequency vibration in track operation with high-speed trains.". Quarterly Reports 1997;18(3):22–7.
[42] Xu L, Lu T. Influence of track flexibility and spatial coherence of track irregularity on vehicle-slab track interaction: frequency-domain analysis. Int J Rail Transp 2021;9(4):342–67.
[43] Xu L, Liu HB, Yu ZW. A coupled model for investigating the interfacial and fatigue damage evolution of slab tracks in vehicle-track interaction. Appl Math Model 2022;101:772–90.
[44] Li Z, Liu HB, Yu ZW. An efficient model for vehicle-track-soil dynamic interaction based on Green's function, cyclic calculation and multi-time-step solution methods. Appl Math Model 2024;126:105–29.
[45] Li Z, Wang WD, Zhang JF, et al. On use of train-track-subgrade dynamic model for investigating the train-induced cumulative deformation of subgrade and its dynamic effects. Appl Math Model 2024;127:71–95.
[46] Gou HY, Gao H, Ban XL, et al. Vibration energy transmission in high-speed train-track-bridge coupled systems. Eng Struct 2023;297(7):117019.
[47] Lei SM, Ge YJ, Li Q, et al. Frequency-domain method for non-stationary stochastic vibrations of train-bridge coupled system with time-varying characteristics. Mech Syst Signal Process 2023;183:109637.